Journal Pre-proof

Whisker-Inspired and Self-Powered Triboelectric Sensor for Underwater Obstacle Detection and Collision Avoidance

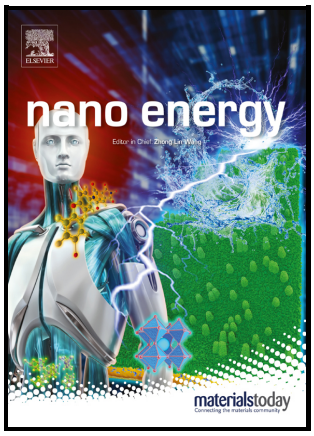

Jianhua Liu, Peng Xu, Jiaxi Zheng, Xiangyu Liu, Xinyu Wang, Siyuan Wang, Tangzhen Guan, Guangming Xie, Minyi Xu

PII: S2211-2855(22)00711-X

DOI: https://doi.org/10.1016/j.nanoen.2022.107633

Reference: NANOEN107633

To appear in: *Nano Energy*

Received date: 19 May 2022
Revised date: 6 July 2022
Accepted date: 24 July 2022

Please cite this article as: Jianhua Liu, Peng Xu, Jiaxi Zheng, Xiangyu Liu, Xinyu Wang, Siyuan Wang, Tangzhen Guan, Guangming Xie and Minyi Xu, Whisker-Inspired and Self-Powered Triboelectric Sensor for Underwater Obstacle Detection and Collision Avoidance, *Nano Energy,* (2022) doi:https://doi.org/10.1016/j.nanoen.2022.107633

Whisker-Inspired and Self-Powered Triboelectric Sensor for Underwater Obstacle Detection and Collision Avoidance

Jianhua Liu[1]†, Peng Xu[1]†*, Jiaxi Zheng[2]†, Xiangyu Liu[1,4], Xinyu Wang[1], Siyuan Wang[1], Tangzhen Guan[1], Guangming Xie[3]*, Minyi Xu[1]*

[1] Dalian Key Lab of Marine Micro/Nano Energy and Self-powered Systems, Marine Engineering College, Dalian Maritime University, Dalian, 116026, China

[2] Transportation Engineering College, Dalian Maritime University, Dalian 116026, China

[3] Intelligent Biomimetic Design Lab, College of Engineering, Peking University, Beijing 100871, China

[4] State Key Laboratory of Physical Chemistry of Solid Surfaces, College of Chemistry and Chemical Engineering, Innovation Laboratory for Sciences and Technologies of Energy Materials of Fujian Province (IKKEM), Xiamen University, Xiamen 361005, China.

†These authors contributed equally to this work.

*Address correspondence to pengxu@dlmu.edu.cn, xiegming@pku.edu.cn, xuminyi@dlmu.edu.cn

Abstract: As key devices for underwater robot to perceive underwater environments, tactile sensors play an important role in seabed exploration. Inspired by the structure of marine mammal whiskers, we designed a bio-inspired whisker sensor (BWS) based on triboelectric nanogenerators to assist underwater robots in sensing underwater environments. The proposed device generated electrical signals through triboelectric and electrostatic induction between a fluorinated ethylene propylene film and ink. With the assistance of a structural design inspired by biology, the artificial BWS could estimate the external stimulation area. We demonstrated specific functions of the sensor, such as LED lights control and real-time external load monitoring to demonstrate its utility. Moreover, the BWS installed in underwater robots identify the direction, position, and frequency of external loads by extracting the characteristics of electrical signals, particularly in cases when optical and acoustic devices cannot be used, such as in turbid water. The results showed that the BWS can serve as an underwater whisker sensor for underwater robots for perceiving underwater

environment and avoiding reactive obstacles.

Key Words: Bio-Inspired Whisker Sensor; Self-Powered; Tactile Perception; Triboelectric Nanogenerator

1. Introduction

Underwater robots are used to assist humans and improve their efficiency in continuous exploration of marine ecosystems [1–5]. Underwater robots are typically equipped with sensors to perform various underwater tasks, such as underwater mapping [6], underwater pipeline detection [7,8], underwater rescue [9–11], and motion tracking [12],[13]. However, when underwater robots operate in an environment with poor water quality, accurate surrounding environmental information can be difficult to obtain, resulting in a significant decrease in their working efficiency [14,15]. Therefore, developing sensors that can improve the perception ability of underwater robots is crucial.

Marine animals often experience changes in their surrounding environment using their sensory organs [16]. For example, seals can track vortex wakes left by other moving fish even when aural and visual clues are suppressed [17]. As a representative marine mammal, sea otters also have highly sensitive sensory organs [18,19]. Whiskers have become important organs for sea otters to obtain external information, especially in dark and turbid underwater environments. When the whiskers of a sea otter come into contact with the surrounding environment, the whiskers cause the hair follicle structure to trigger the reaction in the tentacle nerve. The brain will receive information. Sea otters rely on tactile sensing systems to easily perceive their surrounding environment. Therefore, it is particularly important to develop a tactile sensor that can support the environmental perception of underwater robots. Specifically, the coupling of tactile and visual sensors can significantly improve the environmental recognition accuracy of underwater robots.

Triboelectric nanogenerators (TENGs) have gained significant attention as emerging electromechanical conversion technologies owing to their low power consumption and light weight [20–22]. TENGs combined with triboelectric charging

and electrostatic induction have demonstrated advantages in low-frequency energy harvesting [23–26] and self-powered mechanical sensing [28–34]. In particular, a variety of smart sensors based on the working principle of TENGs have been fabricated to monitor information in the maritime domain, including the liquid level information of berthing ships [40], rolling inclination of running ships [41], operating conditions of the ships' equipment [422,43], and changes in waves [444–46]. In addition, highly sensitive underwater whisker sensors can provide support for underwater robots, allowing them to collect information about the surrounding environment. Therefore, a highly sensitive whisker sensor could be developed by combining the TENG principle with the bionic structure of sea-otter whiskers.

In this study, we designed a bio-inspired whisker sensor (BWS) based on TENGs for underwater robots for perceiving the surrounding environment. The main components of a BWS include a carbon fiber rod for sensing the surrounding environment, an epoxy resin base with good waterproof sealing performance, and four sensing units that convert mechanical signals into electrical signals, as shown in Figure 1. We chose fluorinated ethylene propylene (FEP) film and ink. Charge transfer occurs when these two materials come into contact and then separate, causing the sensing unit to generate a corresponding electrical signal. In particular, when the BWS installed on an underwater robot comes into contact with the surrounding environment, the carbon fiber rod causes the octagonal prism to impact the sensing unit, thereby generating an electrical signal. The underwater robot then senses the orientation and load information based on the electrical signals transmitted by the four sensing units in the BWS. Therefore, this BWS can improve the environmental perception abilities of underwater robots.

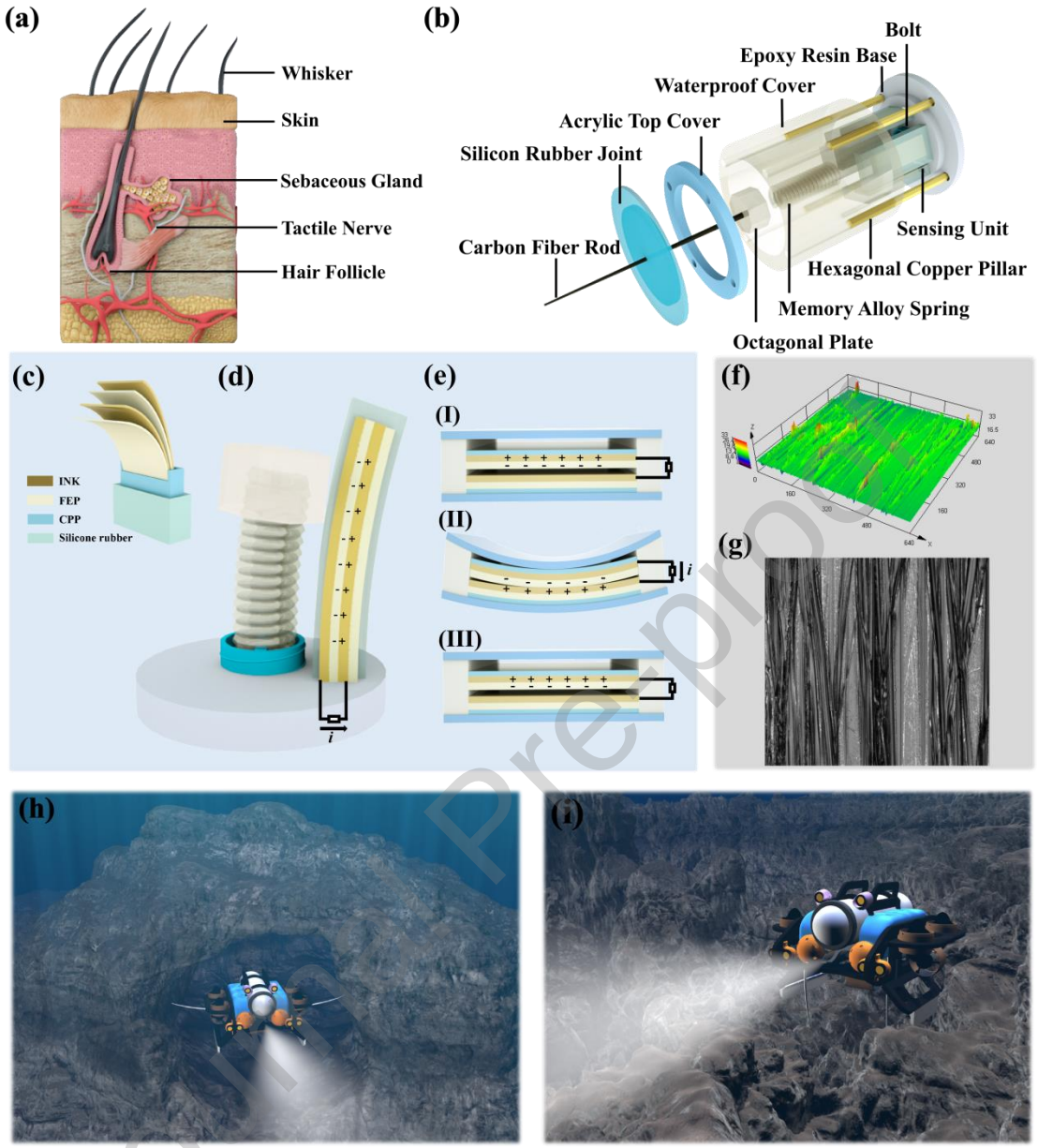

Figure 1. Structure, principle and application of the BWS. (a) Structure of sea otter beard. (b) Exploded view of the BWS. (c) Structure diagram of the sensing unit. (d) Force diagram of the BWS sensing unit. (e) The BWS power generation schematic diagram. (f) Surface roughness of dielectric FEP. (g) Electron micrograph of dielectric material FEP surface. (h) BWS installed on the underwater robot sensing the underwater environment. (i) BWS installed on the underwater robot sensing the seabed surface.

2. Results and Discussion

Inspired by the structure of sea otter whiskers, a BWS was designed to perceive

the surrounding environment of underwater robots, as shown in Figure 1(a). Typically, when the whiskers exposed on the outer layer of the skin are stimulated, tactile nerves will receive signals and send them to the brain. Sea otters use this information to identify their surroundings. Figure 1(b) shows the exploded structural view of the BWS, which consisted of a base made of epoxy resin with good water tightness and corrosion resistance, waterproof cover ($r = 35\ mm\ and\ H = 66\ mm$) fixed on the base using four hexagonal copper pillars, silicone rubber joint fixed to the top of the waterproof cover through the acrylic top cover, waterproof cover and acrylic top cover to prevent water leakage, silicone rubber joint to maintain the orientation of the carbon fiber rod on the octagonal plate, a memory alloy spring to center the carbon fiber rod, and bolt to adjust the height of the memory alloy spring and the four sensing units. The ink and FEP employed improved the output performance of the sensing unit, as shown by the comparative experiments in Figure S1. As shown in Figure 1(c), the sensing unit ($\mathrm{L} = 35\ mm, w = 20\ mm, and\ H = 9mm$) was composed of a cast polypropylene (CPP) film with an electrostatic shielding effect, an FEP film with strong electronegativity, ink and a silicone rubber with good water tightness. The fabrication of the sensing unit is illustrated in Figure S2. The epoxy resin base and waterproof cover and acrylic top cover were attached by hexagonal copper pillars. The silicone rubber joint was fixed to the acrylic top cover. Subsequently, the carbon fiber rod, octagonal plate, memory alloy spring, and bolt on the epoxy resin base were attached in turn. Sensing units were installed vertically around the epoxy resin base. When the BWS was exposed to a complex surrounding environment, the carbon fiber rod deformed to varying degrees, causing the octagonal plate to strike the sensing unit. The sensing unit was deformed after being struck, and the internal dielectric material was electrified by contact. As shown in Figure 1(d), the contact of the dielectric materials inside the deformed sensing unit led to charge transfer, which generated an electrical signal. Figure 1(e) shows the electron transfer process of the sensing unit under external stimuli. State I in Figure 1(e) shows the original state of the sensing unit. As shown in State II of Figure 1(e), when the FEP film and ink came into contact, the electron clouds on the two electrodes overlapped. Because the electronegativity of

FEP is higher than that of ink, free electrons in the ink entered the deeper potential well of the FEP film. In other words, the free electrons in the ink were transferred to the lowest molecular orbital at the FEP interface. When the BWS removed the external load, the FEP film separated from the ink electrode. Because the negative and positive friction charges no longer coincided on the same plane, a dipole moment and potential were generated between the two contact surfaces. Therefore, free electrons were transferred through an external circuit, balancing the local electric field and generating a positive charge on the conductive ink electrode. The electrons continued to flow until the distance between the two contact surfaces returned to State III. As shown in Figure S3, the potential distribution between the two dielectric materials was simulated using COMSOL software, and the working principle of the sensing unit was verified.

In the experiment, we observed the FEP film treated with surface microstructures using a 3D measuring laser microscope, as shown in Figure S4. The treated FEP film produced many groove areas, as shown in Figure 1(f), which increased the surface roughness of the FEP film. This increased the contact area of the two dielectric materials when they were in contact with each other, thus improving the sensitivity of the sensing unit. When the sensing unit was under loading, the internal dielectric material was fully in contact, thereby increasing electron transfer. Therefore, the sensitivity of the BWS improved. In addition, the actual state of the surface microstructure-treated FEP film was scanned using an electron microscope, as shown in Figure 1(g). Figures S5–S8 show the effects of different microprocessing degrees on the roughness of the film surface.

Figure 1(h) shows the application of the BWS to underwater robots for environmental perception. When the underwater robot passed through a complex underwater environment, the BWS provided real-time surrounding environmental information, to ensure that the underwater robot body was not damaged. Figure 1(i) shows the application of the BWS in detecting the seabed surface conditions. The underwater robot collects seabed landform information through the signals transmitted by the BWS, which is beneficial to the effective development of

submarine projects, such as pipeline laying. The development of whisker sensors provides strong support for improving the environmental perception ability of underwater robots.

3. Experiments

To study the performance of the BWS, we conducted experiments on three physical parameters: the load frequency, load displacement, and contact position. As shown in Figure S9, the BWS was installed on a linear motor platform with a pressure sensor, and the electrical signal output of the BWS was collected using a high-resistance electrometer and then visualized through LabVIEW using a computer. The experimental parameters are illustrated in Figure 2(a) to better describe them. The distance from the touch position of the carbon fiber rod to the sensor base was denoted as H. The deformation occurred when the carbon fiber rod was subjected to an external load. The displacement moved by the point of force was A, and the deflection angle was α ($tan\alpha = A / H$). Because the fabrication methods for the four sensing units of the sensor were identical, we studied the laws for a single sensing unit only. We measured the short-circuit current under different contact frequencies when the contact position was $H = 40\,mm$, and the displacement was $A = 11\,mm$.

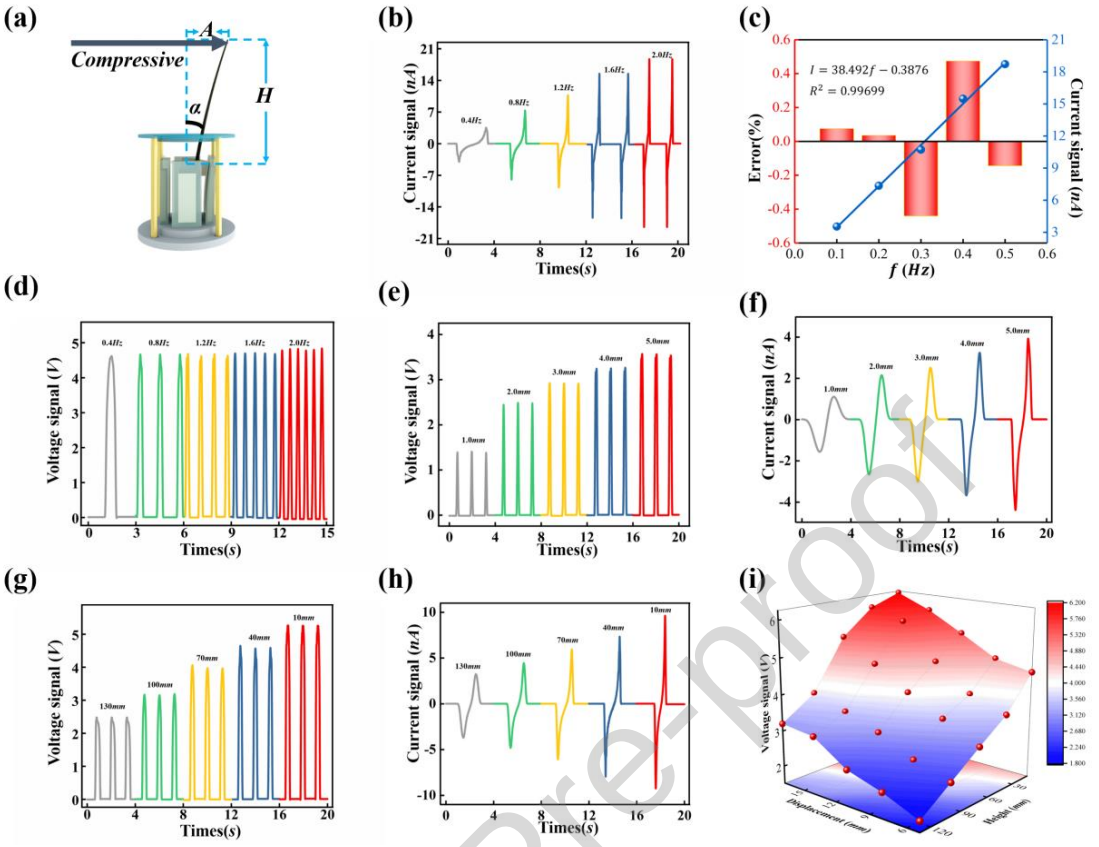

Figure 2. Performance of the BWS under difference load parameters. (a) BWS state under external load. (b) Response range of short-circuit current to external load frequency from 0.4 to 2.0 Hz. (c) Fitting linear relationship between short-circuit current and external load frequency. (d) Response range of open-circuit voltage to external load frequency from 0.4 to 2.0 Hz. (e) Response range of open-circuit voltage to external load displacement from 1.0 to 5.0 mm. (f) Response range of short-circuit current to external load displacement from 1.0 to 5.0 mm. (g)Response range of open-circuit voltage to external load height from 130 to 10 mm. (h) Response range of short-circuit current to external load height from 130 to 10 mm. (i) Influence of external load frequency and external load height on open-circuit voltage.

Figure 2(b) shows that when the contact frequency increased from 0.4 to 2.0 Hz, the short-circuit current of the sensing unit increased from 3.81 to 18.6 nA. As shown in Figure 2(c), we used the leave-one-out cross-validation (LOOCV) strategy to obtain the relationship between short-circuit current and external stimuli, $I = 38.492f - 0.3876$, $R^2 = 0.99699$, where the correlation coefficient R^2 indicated that the external load and output current had an approximately linear relationship,

with an error of less than 0.02 % at magnitude $f = 0.2\,Hz$, and a relatively higher error of 0.44 % at magnitude $f = 0.3\,Hz$. These errors were possibly caused by the high-frequency vibrations generated by the linear motor. Figure 2(d) shows the changes in the open-circuit voltage from 0.4 to 2.0 Hz under the conditions of $H = 40\,mm$ and $A = 11\,mm$. Simultaneously, we also tested at a frequency of 3.0 Hz and obtained almost the same effect, as shown in Figure S10. Interestingly, we found that the open-circuit voltage of the sensing unit was maintained at 4.6 V, and was not affected by frequency. Thus, the higher the loading frequency, the faster the contact separation of the dielectric material inside the sensing element, and some electrons accumulated without transfer. Therefore, the short-circuit current increased, and we determined that the BWS could adapt to the high-frequency state. Then, we tested the open-circuit voltage under different displacements at $f = 0.8\,Hz$ and $H = 40\,mm$. As shown in Figure 2(e), when the displacement increased from 1.0 to 5.0 mm, the open-circuit voltage of the sensing unit increased from 1.4 to 3.5 V. Figure S11 shows that the linear relationship between the load displacement and open-circuit voltage could be expressed as $U = 0.5119A + 1.1839,\ R^2 = 0.91679$. Figure 2(f) shows the short-circuit current generated by the five different load displacements at $H = 40\,mm$ and $f = 0.8\,Hz$. When the contact frequency increased from 1.0 to 5.0 Hz, the short-circuit current also increased from 1.10 to 3.93 nA. In addition, Figure 2(g) shows the open-circuit voltage generated by different touch positions at $A = 11\,mm$ and $f = 0.8\,Hz$. With decreasing contact height, the dielectric material in the sensing unit increased the contact area, resulting in an increase in the number of electronic exchanges and the strength of the electrical signals. The linear relationship between the contact height and open-circuit voltage could be expressed as $U = -0.02325H + 5.52087,\ R^2 = 0.99281$, as shown in Figure S12. Under this condition, the short-circuit current of the sensing unit increased with decreasing contact height, as shown in Figure 2(h). Furthermore, Figure 2(i) clearly shows the influence of the load displacement and contact height on the output signal of the sensing unit, where the voltage output value of the sensing unit increased with increasing load displacement and decreasing contact height.

Figure S13 shows that the current output value of the sensing unit increased with increasing load displacement and decreasing contact height. Figure S14 shows the effect of the load frequency and load displacement on the short-circuit current. In addition, Figures S15–16 show the effects of the load frequency and contact height on the open-circuit voltage and short-circuit current.

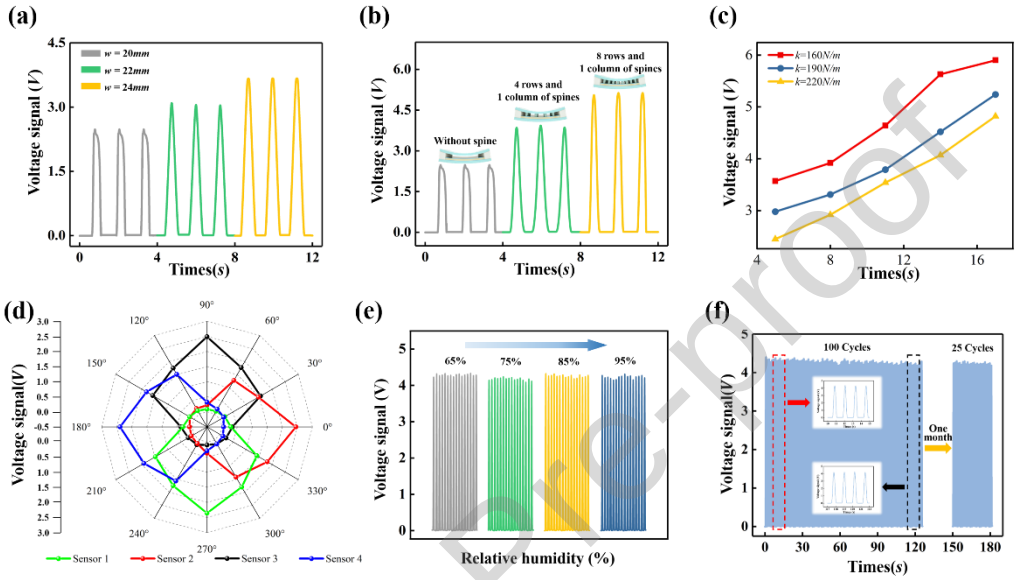

Figure 3. Characterization of the sensing unit. (a) Relationship between sensing unit width and voltage signal output of the BWS. (b) Relationship between the number of spines and the voltage signal output of the BWS. (c) Relationship between spring stiffness coefficient and voltage signal output of the BWS. (d) Directional patterns of the BWS; (e) Relationship between BWS and relative humidity; (f) Durability test diagram of the BWS.

To further improve the sensing performance of the BWS, Figure 3(a) shows the effect of the the sensing unit size on the open-circuit voltage signal at $H = 130\,mm$ and $A = 11\,mm$. As the width of the sensing unit increased from 20 to 24 mm, the open-circuit voltage increased from 2.49 to 4.19 V. This is because the contact area of the two dielectric materials increases when the BWS was subjected to an external load. We then, tested the influence of the distance between the dielectric materials on the output performance of the sensing unit, as shown in Figure S17. The output performance of the sensing unit decreased with distance. This is because the contact area and number of transferred charges decreased as the distance between the

dielectric materials increased. Therefore, the output performance of the sensing unit was reduced. In addition, Figure 3(b) shows the effect of the spine structure on the performance of the sensing unit, in which we tested three types of sensing units with different numbers of spines. The open-circuit voltage of a sensing unit without spines on the inner surface was 2.49 V, whereas that of a sensing unit with four rows and one column of spines on the inner surface was 3.85 V. Furthermore, the sensing unit with eight rows and one column of spines on the inner surface produced an open-circuit voltage of 5.13 V. The increased in the number of spines made the dielectric materials fully in contact with each other, which caused a larger electrical signal for the sensing unit. Subsequently, we studied the effects of three memory alloy springs with different stiffness coefficients on the performance of the BWS. The test was carried out with displacement A from 8 to 17 mm at $f = 0.8\,Hz$ and $H = 40\,mm$. Figure 3(c) shows that the memory alloy spring with a spring stiffness coefficient of 160 N/m had a better electrical signal output than the other two memory alloy springs (190 N/m and 220 N/m). This is because the deflection degree of the memory alloy spring decreased as its stiffness coefficient increased. Therefore, the higher the stiffness coefficient, the smaller the contact area between the two dielectric materials.

Figure 3 (d) shows the voltage signals in different directions for the four sensing units. The signal output decreased gradually with the deviation in the load direction from the sensing unit. Therefore, a BWS installed on the platform of an underwater robot can be used to identify the direction of an external load. Subsequently, the BWS was placed in an environment where the humidity could be adjusted to test its voltage output signal, as shown in Figure S18. Figure 3(e) shows that the output voltage of the BWS remained constant at approximately 4.2 V as the humidity increased from 65 % to 95 %. Therefore, the sensing unit of the BWS can operate normally in environments with different humidity levels. Finally, we conducted a durability test of the BWS, as shown in Figure 3(f). One hundred experimental cycles were performed under the same experimental conditions. The sensing unit of the BWS generally maintained a stable output performance, and the voltage value remained at approximately 4.3 V after a month. In addition, the BWS was tested again for 300

cycles to further verify the stability of its output performance (Figure S19). The BWS was proven to have a more durable performance.

4. Demonstration of the BWS

4.1 Real-time Control

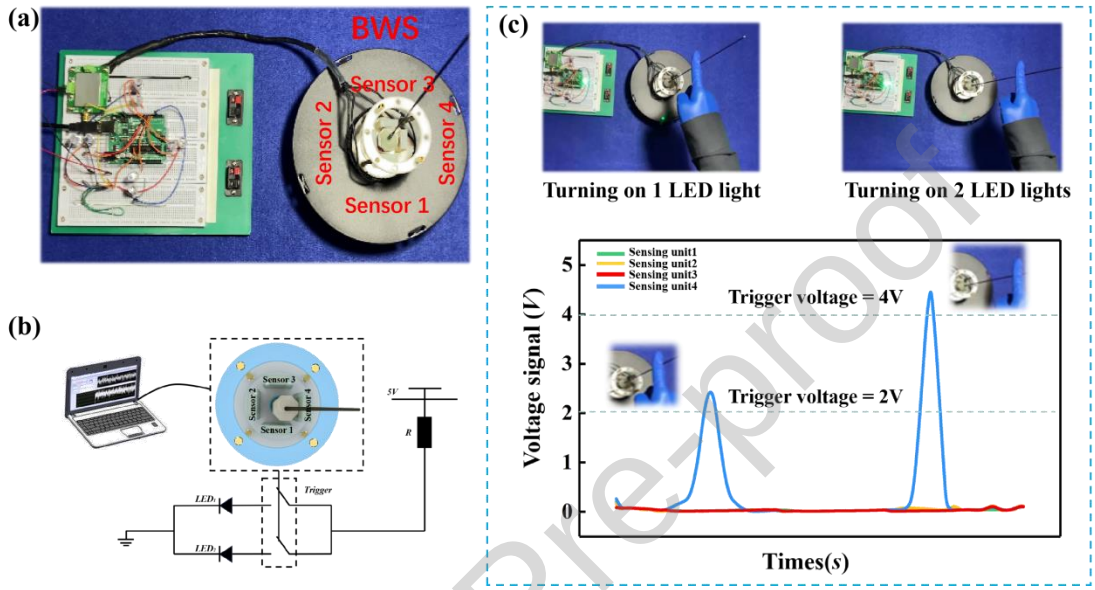

Figure 4. Application of the BWS in real-time control. (a) Schematic of the experimental electronic setup. (b) Electronic module used for controlling light-emitting diode (LED) lights. (c) Demonstration of the BWS as a load switch control and its corresponding output voltage signal.

A circuit diagram for lighting the light-emitting diodes (LEDs) in the experiment using the BWS is shown in Figure 4(a). The experimental setup used an Arduino board to collect signals and process the data. It is noteworthy that there were two LEDs in each direction, and the number of lighted LEDs indicated the peak voltage magnitude of the BWS. The operator used different load magnitudes to drive the whisker rod in four directions, which generated electrical pulses to light up the corresponding LED. Figure 4(b) shows the experimental electron diagram of the BWS, taking sensing unit 4 as an example. As shown in Fig. 4(c), when the operator applied a load to the BWS, the sensing unit generated an electrical signal. Moreover, the voltage value of the BWS reached the preset trigger value, thus driving the LED light, where the number of lighted LEDs depended on the magnitude of the peak voltage

(see Supplementary Movie S1). The BWS identified the magnitude of the external load through the voltage signal, confirming that it had a good environmental sensing ability.

4.2 External Load Monitoring

To further reflect the monitoring ability of the BWS based on whisker deflection angle, we designed a visual interface using MATLAB to display the whisker deflection angle, utilizing the output voltage of the BWS in real time. A logic block diagram for the monitoring of the whisker deflection angle is shown in Figure 5(a). When the Arduino collected the output voltage from the BWS, it processed the data in combination with the previous fitting model, followed by the transmission to the MATLAB visual interface. Figure 5(b) shows the experimental setup in which the BWS was fixed on the optical plate, and different external loads were simulated by adjusting the stroke of the linear motor. Figure 5(c) shows the specific content of the visual interface image. When the BWS was loaded in different directions, the corresponding directions displayed real-time information of the load displacement and whisker deflection angle. Only sensing unit 4 was used for demonstration because the principles applied for all directions were similar. The BWS exhibited a good load-sensing ability (see Supplementary Movie S2).

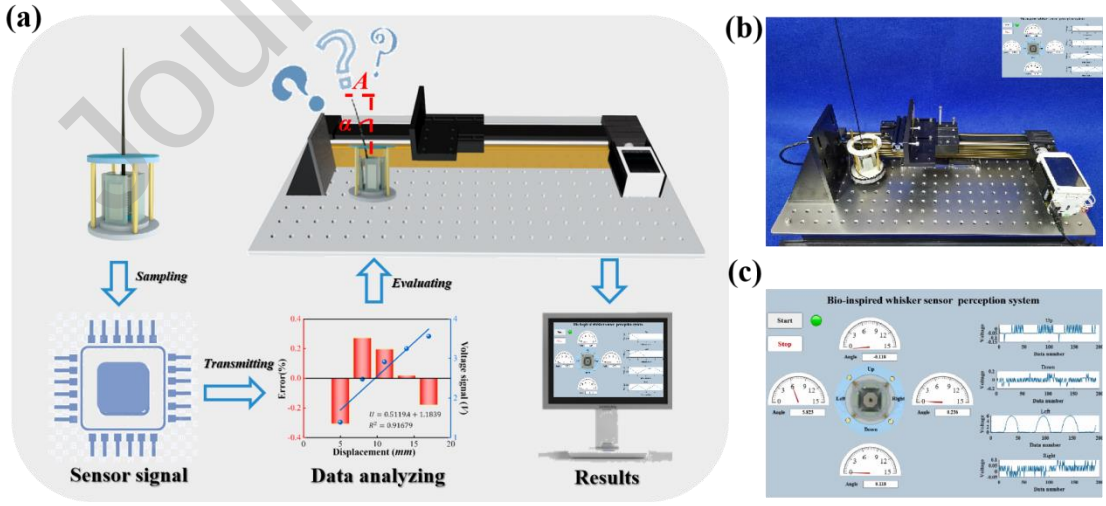

Figure 5. Application of the BWS in external load monitoring. (a) Logic block diagram used to show the BWS realizes load displacement monitoring. (b) Schematic of the visualization interface and experimental setup. (c) Data collected by Arduino.

4.3 Application of the BWS for Reactive Obstacle Avoidance

The BWS was installed on the head of an underwater robot, as shown in Figure 6(a). To demonstrate the reactive obstacle avoidance ability of the underwater robot equipped with the BWS, we placed a 1.6 m × 0.8 m × 0.8 m water tunnel, assembled from a transparent acrylic plate in an indoor pool (5 m × 3 m × 2 m), as shown in Figure 6(b). The locations of the underwater obstacles are shown in Figure 6(c). The entrance of the water tunnel consisted of Obstacle 1, and the triangular prism on the upper wall of the water tunnel was Obstacle 2. When the underwater robot moved towards the entrance of the water tunnel, the BWS first collided with the upper wall of the water tunnel, generating an electrical signal, then the underwater robot reduced the dive depth after acquiring this information. After two adjustments, the underwater robot smoothly entered the water tunnel. When the BWS sensed the Obstacle 2 in the tunnel, the underwater robot adjusted the diving depth according to the previous method, and smoothly passing the obstacle. Figure 6(d) shows the specific shape of the BWS and real-time voltage signal as the underwater robot avoided these two obstacles. The general environmental information of the water tunnel was recognized by the BWS (see Supplementary Movie S4). However, the underwater robot could not recognize the environment at the bottom of the water tunnel because no BWS was installed at the bottom of the underwater robot. Consequently, the underwater robot could not recognize and avoid obstacles at the bottom of the water tunnel. Thus, it could not pass smoothly.

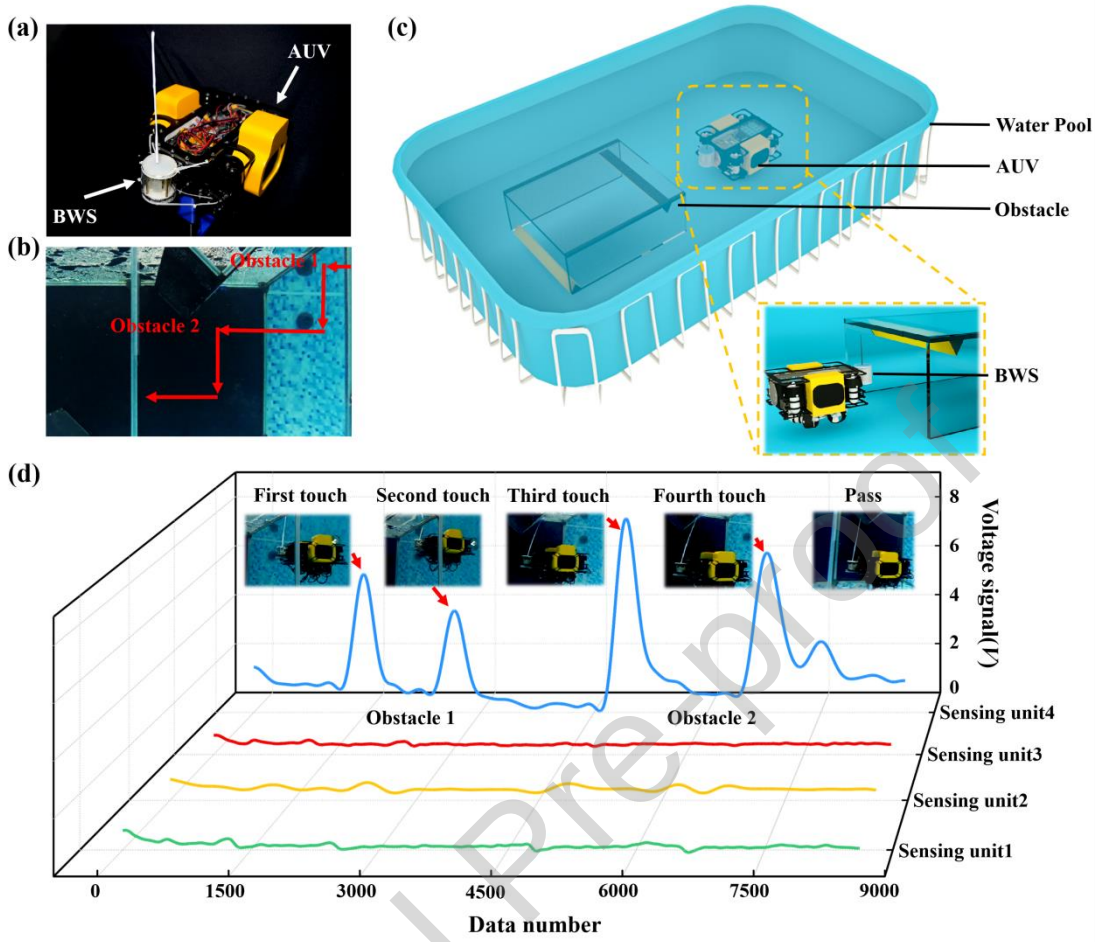

Figure 6. Experiment with the BWS mounted on underwater robot. (a) - (c) Sensor configuration and experimental scene layout during reactive obstacle avoidance using BWS. (d) The BWS output signal for underwater reactive obstacle avoidance.

4.4 Application of the BWS in Underwater Environment Detection

Furthermore, we explored the ability of the BWS to perceive environmental information. Figure 7(a) shows the specific conditions of the underwater environment obtained after data analysis, which was conducted by collecting and processing the electrical signals generated by the BWS. As shown in Figure 7(b), the underwater robot was operated in the remote guidance mode at the beginning of the mission and advanced near the water tunnel. When the BWS contacted the upper edge of the water tunnel, the underwater robot started to detect the environment of the water tunnel at a constant speed. During the detection process, the non-uniformity of the wall of the water tunnel was determined based on the rising or falling edge of the signal (see Supplementary Movie S4). Thus, the experimental results demonstrated that the

underwater robot has a high potential for environmental detection.

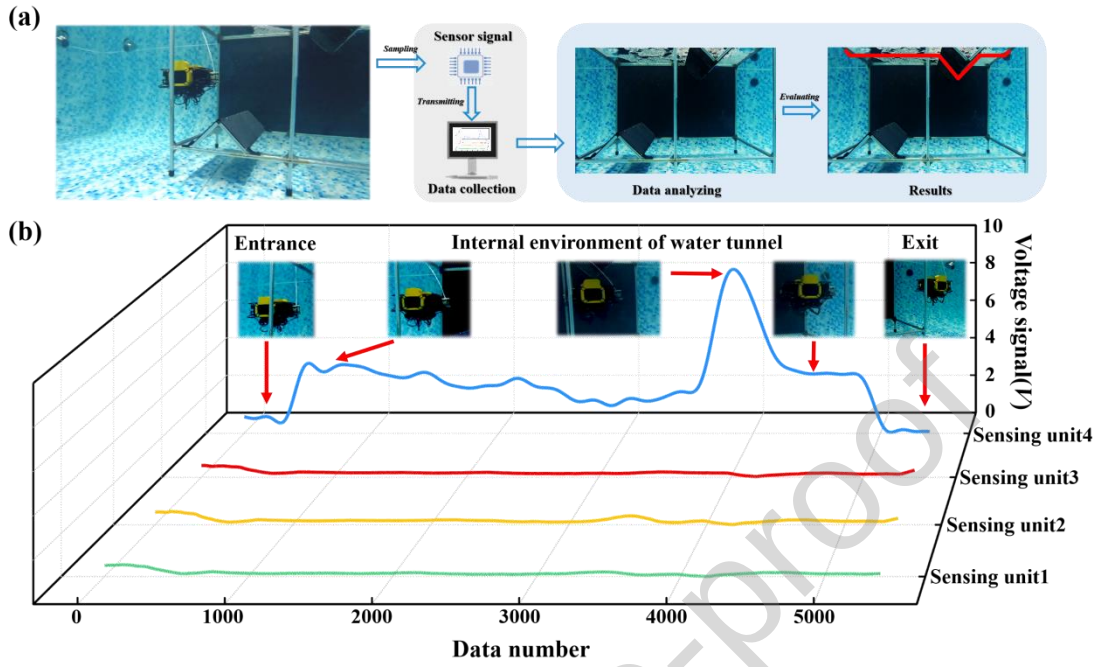

Figure 7. Experiment with the underwater detection of the BWS. (a) Flow chart of the BWS for underwater environment detection. (b) The application of the BWS in underwater environment detection and its corresponding output voltage signal are demonstrated.

5. Conclusions

In this study, a BWS based on a triboelectric nanogenerator was designed and used as an underwater sensing system for underwater robots. The dielectric material in the sensing unit generated electrical signals via contact separation. The height, displacement and frequency of an external load was analyzed by fitting a linear relationship between it and the electrical signal. In addition, the sensing unit with spine structure and a spring with a smaller stiffness coefficient improved the sensing sensitivity of the BWS. The experiments demonstrated that the BWS is durable and can adapt to complex environments. The BWS was used to control the on/off states of the light-emitting diodes in different directions, and the external signals generated by the BWS were displayed in real time using the MATLAB visual interface. The test results indicate that an underwater robot equipped with the BWS can detect the surface conditions of underwater tunnels and autonomously avoid the obstacles.

Therefore, this BWS has a high potential for underwater environment perception.

6. Experimental Section

6.1 Preparation of the BWS

The constituent materials of the triboelectric sensing unit included Dragon Skin, CPP, FEP, and ink. Fifty milliliters of Dragon Skin A and 50 ml of Dragon Skin B in a ratio of 1:1 were mixed in a Petri dish. Then, the mixture was evacuated to 0.1 MPa using a vacuum pump. The mixture was poured into a 3D printed mold and allowed to sit for 24 h. The bottom 3 mm thick silicone substrate and the top 2 mm thick silicone layer were both made of Dragon Skin. The 1 mm thick commercial product CPP in the middle was cut into rectangles (30 mm long, 18 mm wide) using a utility knife. A conductive ink was sprayed on a 0.3 mm thick FEP film, which served as a dielectric layer. In addition, the silicone rubber joint was made of Dragon Skin, and the top cover made of polylactic acid was 3D printed. The epoxy base was mixed with a 5:1 curing agent, and the mixture was evacuated to 0.1 MPa with a vacuum pump to obtain the epoxy base. The carbon fiber rod was then fixed to the top of the octagonal prism with hot melt glue, and the memory alloy spring was fixed to the bottom of the octagonal prism. Finally, the epoxy base, waterproof cover, silicone rubber joint, and acrylic top cover with hexagonal copper pillars.

6.2 Electrical Measurement of the BWS

The surface morphology of the micro-tank structured FEP film of the spray conductive ink was characterized using a 3D measuring laser microscope. To measure the electrical signal of the BWS, a collision experiment was performed using an integrated linear motor (R-LP3). Different loads were simulated using the touchscreen adjustment parameters on the linear motor. The voltage signal was measured using a Keithley (6514) electrostatic meter. Ni-6259 was used for data collection. The software platform was based on LabVIEW build and was implemented for real-time data acquisition control and analysis. When the BWS collided with an integrated linear motor, the Keithley electrostatic meter sampled the electrical signal and

transmitted the data to the computer, and visualized the LabVIEW software.

Acknowledgments

The authors would like to thank the National Key R & D Project from the Minister of Science and Technology (2021YFA1201604), the Dalian Outstanding Young Scientific and Technological Talents Project (2021RJ11), the National Natural Science Foundation of China (51879022), the Beijing Natural Science Foundation (No. 4192026).

Conflict of Interest

The authors declare no conflict of interest.

Reference

[1] Frey C L, Wood S L. Development of an autonomous underwater vehicle for sub-ice environmental monitoring in Prudhoe Bay, Alaska[M]. IEEE, 2003.

[2] Yu J, Zhang A, Li Z, et al. The development and the challenges of underwater vehicles for polar expedition[C]//Proceedings of the 2004 International Symposium on Underwater Technology (IEEE Cat. No. 04EX869). IEEE, 2004: 95-99.

[3] Stopforth R, Holtzhausen S, Bright G, et al. Robots for Search and Rescue Purposes in Urban and Underwater Environments-a survey and comparison[C]//2008 15th International Conference on Mechatronics and Machine Vision in Practice. IEEE, 2008: 476-480.

[4] Listak M, Martin G, Pugal D, et al. Design of a semiautonomous biomimetic underwater vehicle for environmental monitoring[C]//2005 International Symposium on Computational Intelligence in Robotics and Automation. IEEE, 2005: 9-14.

[5] Liu J, Zheng J, Xu P, et al. Development of AUV Mechatronics Integration for Underwater Intervention Tasks[C]//2021 6th International Conference on Automation, Control and Robotics Engineering (CACRE). IEEE, 2021: 322-326.

[6] Wang Y, Ji Y, Woo H, et al. Three-dimensional underwater environment reconstruction with graph optimization using acoustic camera[C]//2019 IEEE/SICE International Symposium on System Integration (SII). IEEE, 2019: 28-33.

[7] Jiang C, Wan L, Sun Y. Design of motion control system of pipeline detection AUV[J]. Journal of Central South University, 2017, 24(3): 637-646.

[8] Wang X L, Li L, Cui Y X. Detection and Location of Underwater Pipeline based on Mathematical Morphology for an AUV[C]//Key Engineering Materials. Trans Tech Publications Ltd, 2013, 561: 591-596.

[9] Fattah S A, Abedin F, Ansary M N, et al. R3Diver: Remote robotic rescue diver for rapid underwater search and rescue operation[C]//2016 IEEE Region 10 Conference (TENCON). IEEE, 2016: 3280-3283.

[10] Holtzhausen S, Matsebe O, Tlale N S, et al. Autonomous underwater vehicle motion tracking using a Kalman filter for sensor fusion[C]//2008 15th International Conference on Mechatronics and Machine Vision in Practice. IEEE, 2008: 103-108.

[11] Birk A, Wiggerich B, Bülow H, et al. Safety, security, and rescue missions with an unmanned aerial vehicle (UAV)[J]. Journal of Intelligent & Robotic Systems, 2011, 64(1): 57-76.

[12] Matos A, Martins A, Dias A, et al. Multiple robot operations for maritime search and rescue in euRathlon 2015 competition[C]//OCEANS 2016-Shanghai. IEEE, 2016: 1-7.

[13] C. Lee, "MEMS/NEMS based enabling technologies for self-sustained wireless sensor nodes," 2013 IEEE MTT-S International Microwave Workshop Series on RF and Wireless Technologies for Biomedical and Healthcare Applications (IMWS-BIO), 2013, pp. 1-3, doi: 10.1109/IMWS-BIO.2013.6756260.

[14] Muscolo G G, Cannata G. A novel tactile sensor for underwater applications: Limits and perspectives[C]//OCEANS 2015-Genova. IEEE, 2015: 1-7.

[15] Li T, Rong S, Cao X, et al. Underwater image enhancement framework and its application on an autonomous underwater vehicle platform[J]. Optical

Engineering, 2020, 59(8): 083102.

[16] Dehnhardt G, Hyvärinen H, Palviainen A, et al. Structure and innervation of the vibrissal follicle-sinus complex in the Australian water rat, Hydromys chrysogaster[J]. Journal of Comparative Neurology, 1999, 411(4): 550-562.

[17] Wang S, Xu P, Wang X, et al. Underwater bionic whisker sensor based on triboelectric nanogenerator for passive vortex perception[J]. Nano Energy, 2022: 107210.

[18] Strobel S M K, Sills J M, Tinker M T, et al. Active touch in sea otters: in-air and underwater texture discrimination thresholds and behavioral strategies for paws and vibrissae[J]. Journal of Experimental Biology, 2018, 221(18): jeb181347.

[19] Strobel S M K, Miller M A, Murray M J, et al. Anatomy of the sense of touch in sea otters: Cutaneous mechanoreceptors and structural features of glabrous skin[J]. The Anatomical Record, 2022, 305(3): 535-555.

[20] Fan F R, Tian Z Q, Wang Z L. Flexible triboelectric generator[J]. Nano energy, 2012, 1(2): 328-334.

[21] Luo J, Wang Z L. Recent progress of triboelectric nanogenerators: From fundamental theory to practical applications[J]. EcoMat, 2020, 2(4): e12059.

[22] Zhu J, Zhu M, Shi Q, et al. Progress in TENG technology—A journey from energy harvesting to nanoenergy and nanosystem[J]. EcoMat, 2020, 2(4): e12058.

[23] Wang Z L, Jiang T, Xu L. Toward the blue energy dream by triboelectric nanogenerator networks[J]. Nano Energy, 2017, 39: 9-23.

[24] Xie W, Gao L, Wu L, et al. A nonresonant hybridized electromagnetic-triboelectric nanogenerator for irregular and ultralow frequency blue energy harvesting[J]. Research, 2021, 2021.

[25] Wang Y, Liu X, Chen T, et al. An underwater flag-like triboelectric nanogenerator for harvesting ocean current energy under extremely low velocity condition[J]. Nano Energy, 2021, 90: 106503.

[26] Liang X, Liu Z, Feng Y, et al. Spherical triboelectric nanogenerator based on

spring-assisted swing structure for effective water wave energy harvesting[J]. Nano Energy, 2021, 83: 105836.

[27] Xia K, Fu J, Xu Z. Multiple-frequency high-output triboelectric nanogenerator based on a water balloon for all-weather water wave energy harvesting[J]. Advanced Energy Materials, 2020, 10(28): 2000426.

[28] Xu P, Wang X, Wang S, et al. A triboelectric-based artificial whisker for reactive obstacle avoidance and local mapping[J]. Research, 2021, 2021.

[29] Guo X, He T, Zhang Z, et al. Artificial intelligence-enabled caregiving walking stick powered by ultra-low-frequency human motion[J]. ACS nano, 2021, 15(12): 19054-19069.

[30] Wang Z, An J, Nie J, et al. A Self-powered angle sensor at nanoradian-resolution for robotic arms and personalized medicare[J]. Advanced Materials, 2020, 32(32): 2001466.

[31] Zou Y, Tan P, Shi B, et al. A bionic stretchable nanogenerator for underwater sensing and energy harvesting[J]. Nature Communications, 2019, 10(1): 1-10.

[32] Zhao C, Liu D, Wang Y, et al. Highly-Stretchable rope-like triboelectric nanogenerator for self-powered monitoring in marine structures[J]. Nano Energy, 2022: 106926.

[33] Xu M, Wang P, Wang Y C, et al. A soft and robust spring based triboelectric nanogenerator for harvesting arbitrary directional vibration energy and self-powered vibration sensing[J]. Advanced Energy Materials, 2018, 8(9): 1702432.

[34] Xu P, Liu J, Liu X, et al. A bio-inspired and self-powered triboelectric tactile sensor for underwater vehicle perception[J]. npj Flexible Electronics, 2022, 6(1): 1-10.

[35] Sayegh M A, Daraghma H, Mekid S, et al. Review of Recent Bio-Inspired Design and Manufacturing of Whisker Tactile Sensors[J]. Sensors, 2022, 22(7): 2705.

[36] Shi Q, Wu H, Wang H, et al. Self-powered gyroscope ball using a triboelectric mechanism[J]. Advanced Energy Materials, 2017, 7(22): 1701300.

[37] Zhu J, Zhu M, Shi Q, et al. Progress in TENG technology—A journey from energy harvesting to nanoenergy and nanosystem[J]. EcoMat, 2020, 2(4): e12058.

[38] Zhu M, Yi Z, Yang B, et al. Making use of nanoenergy from human-Nanogenerator and self-powered sensor enabled sustainable wireless IoT sensory systems[J]. Nano Today, 2021, 36: 101016.

[39] An J, Chen P, Wang Z, et al. Biomimetic hairy whiskers for robotic skin tactility[J]. Advanced Materials, 2021, 33(24): 2101891.

[40] Zhang X, Yu M, Ma Z, et al. Self-powered distributed water level sensors based on liquid–solid triboelectric nanogenerators for ship draft detecting[J]. Advanced Functional Materials, 2019, 29(41): 1900327.

[41] Wang S, Wang Y, Liu D, et al. A robust and self-powered tilt sensor based on annular liquid-solid interfacing triboelectric nanogenerator for ship attitude sensing[J]. Sensors and Actuators A: Physical, 2021, 317: 112459.

[42] Xiao X, Zhang X, Wang S, et al. Honeycomb structure inspired triboelectric nanogenerator for highly effective vibration energy harvesting and self-powered engine condition monitoring[J]. Advanced Energy Materials, 2019, 9(40): 1902460.

[43] Zhao H, Xiao X, Xu P, et al. Dual-tube helmholtz resonator-based triboelectric nanogenerator for highly efficient harvesting of acoustic energy[J]. Advanced Energy Materials, 2019, 9(46): 1902824.

[44] Xu M, Zhao T, Wang C, et al. High power density tower-like triboelectric nanogenerator for harvesting arbitrary directional water wave energy[J]. ACS nano, 2019, 13(2): 1932-1939.

[45] Wang X, Liu J, Wang S, et al. A self-powered triboelectric coral-like sensor integrated buoy for irregular and ultra-low frequency ocean wave monitoring[J]. Advanced Materials Technologies, 2021: 2101098.

[46] Wang H, Fan Z, Zhao T, et al. Sandwich-like triboelectric nanogenerators integrated self-powered buoy for navigation safety[J]. Nano Energy, 2021, 84: 105920.

CRediT authorship contribution statement

Jianhua Liu: Investigation, Software, Data curation, and Writing-review and editing. Peng Xu: Conceptualization, Software, and editing. Jiaxi Zheng: Investigation, Data curation, Software. Xiangyu Liu: Data curation and Software. Xinyu Wang: Investigation and Visualization. Siyuan Wang: Visualization. Tangzhen Guan: Visualization. Guangming Xie: Conceptualization, Methodology and Writing-review. Minyi Xu: Conceptualization, Methodology and Writing-review.

Declaration of interests

☒ The authors declare that they have no known competing financial interests or personal relationships
that could have appeared to influence the work reported in this paper.

☐The authors declare the following financial interests/personal relationships which may be considered
as potential competing interests:

Graphical abstract